Research Article | Vol. 33, No. 12 / 16 Jun 2025 / Optics Express 25767
Optics EXPRESS

Surface discretization in optical aspheres production

FRANCISCO UNAI CAJA,[1,2] SERGIO BARBERO,[3,*] AND MARÍA DEL MAR GONZÁLEZ[1]

[1] Departamento de Matematicas, Universidad Auntónoma de Madrid & ICMAT, 28049 Madrid, Spain
[2] Department of Mathematics, University of Texas at Austin, USA
[3] Instituto de Óptica (CSIC), Serrano 121, Madrid, Spain
[*] sergio.barbero@csic.es

Abstract: Highly aspherical optical surfaces are commonplace in the optical industry today. Surface discretization, i.e., describing the surface via a point cloud or a grid, is crucial in several surface production processes such as machining, finishing, metrology, and characterization. The simplest way to discretize an aspherical surface is to generate a uniform $x-y$ sampling in the vertex plane and orthogonally project that sampling onto the surface. However, such a method leads to excessively non-uniform samplings when the surface is highly aspherical, which is not rare in the current optical industry. To overcome this problem, we have studied the properties of three discretization methods applied to optical aspheres. The first essentially generates the involute of a circle embedded within the optical surface (CI). The other two methods are based on finding an intermediate mapping. Whereas one method finds this mapping by solving a Laplace-Beltrami partial derivatives system (LB), the other uses optimal mass transportation (OT). We compared the outcomes of these methods with the trivial projection method. Evidence shows that, when targeting uniformity, the CI and OT provide the best outcomes. Conversely, the CI and LB methods achieve better results if the quality target has grid cells close to equilateral.

1. Introduction

Surface production is ubiquitously applied in modern industry, covering many applications: optics, aerospace, automotive, etc. It implies a set of techniques such as machining, finishing, metrology, and characterization. Machining creates the surface shape (or the mold from which the surface is fabricated) by controlled material removal from a blank; finishing, a subsequent refinement after machining, aims at minimizing the surface roughness and waviness generated by the rough machining process; surface metrology is the as-built surface measurement and, finally, surface characterization is the mathematical procedure to evaluate the difference between the nominal design and the as-built surface. In all techniques mentioned above, a crucial step is to set a point cloud or grid of points discretizing the surface, referred to as *surface discretization*.

Aspherical surfaces (but still axially symmetric surfaces) are used in many optical applications whenever reduced dimensions and/or good optical quality performance are required. The improvement in the machining techniques of aspherical surfaces has made it possible to produce those with even extreme deviations from best-fit spheres [1]. This machining development inevitably implies a co-development of better optical metrology and characterization procedures. Indeed, in more than a few cases and whenever high-precision lenses are required, measuring and machining are combined in a closed-loop process to improve the final result [1].

Surface metrology can be divided into two major groups: whole-surface or sequentially point-by-point measuring devices. Among the former, the most important, but not the unique, technique is the interferometry-based [1]. In the latter, a probe scans through the surface guided by a computer-numerical-control (CNC) system. Then the process is achieved by defining a set of points within the surface defined by coordinates: $\{x, y, z\}$. Due to limited acceptance angles of

#563446 https://doi.org/10.1364/OE.563446
Journal © 2025 Received 25 Mar 2025; revised 9 May 2025; accepted 9 May 2025; published 9 Jun 2025

Optics EXPRESS

whole surface measurements in high aspheric surfaces, the preferred techniques are those based on pointwise measurements [2]. This work is mostly focused on these.

The pointwise measuring instruments can be classified according to the physical structure of the probe: tactile probe, atomic force microscopy (AFM) tip, optical probe, etc. [3]. Depending on the pointwise measuring device, there are different possible scanning sampling strategies: parallel or radial lines, concentric circles, spiral curves, etc. [3], giving rise to either some type of uniform $x - y$ (Cartesian) or $r - \rho$ rastering scans [3]. In some special cases, statistically based schemes have also been proposed, e.g. Hampsi and Hammersley sampling methods [4,5].

Particularly interesting for our purposes are the spiral-type samplings: an Archimedean [6] and a Fermat [7] spiral have been proposed in contact and no-contact (optical) metrology, respectively. Additionally, a significant group of surface finishing techniques generates a turning-lapping path (diamond cutting tool) obtained by the combination of a rotation movement of the surface to be polished, and axial displacements of the lapping tool [8]. This provides the spiral-type curve as the natural lapping path (sampling curve).

Surface discretization inherently implies the convenience of selecting the set $\{x, y, z\}$ following some optimal criteria. One arises naturally from a quality-based requirement, whereas the other arises from a cost-based guideline. As for the quality, a usual requisite is the homogeneity of the process over the surface, which is translated into the requirement that the net $\{x, y, z\}$ samples the surface in the most uniform way possible. A reasonable and universal cost-based criterion is to minimize the overall operation (finishing or measurement) time. Indeed, in industrial processing production, time must always be optimized because of economic costs and risks of surface damage [3]. Reducing time is also meaningful to lower noise when surface measurement may change with time, for instance, due to external vibrations.

Anyway, the approaches to addressing these two criteria have been different in surface finishing and metrology. In surface metrology, more stress has been put on minimizing measurement time. Conversely, in surface finishing, the concern for uniformity is higher because the goal is to reduce irregularities that are more or less evenly distributed over the surface area (surface roughness).

Conventionally, surface discretization in optical aspheres is constructed using some uniform criteria in the x-y vertex plane (tangent plane to the asphere at its center), neglecting its surface geometry. However, in highly aspheric or curved surfaces, this procedure can lead (as we will show in this paper) to highly non-uniform samplings within the surface; it particularly tends to sample convex surfaces more uniformly in the center than the periphery.

Even without limiting the analysis to optics, not too many alternatives have been presented explicitly considering the surface geometry. For instance, Edgeworth et. al. [9] proposed the so-called adapted sampling, a strategy that considers the surface normal measurements to develop interpolating curves between sample points, a somewhat heuristic approach to the problem. Within spiral-type schemes, Gong et al. [10] proposed to use an Archimedean spiral curve defined on the surface itself instead of on the vertex plane. One should be especially cautious when finding the most optimal spiral-type curve *filling* the asphere. Some of us proved that, for flat curvatures, circle involutes are the best candidates for minimum-time scanning paths maintaining a prescribed measurement accuracy condition [11]. In this paper, we extend that result to optical aspheres, providing an advantageous way to generate curve samplings on those surfaces.

A conceptually appealing way to discretize surfaces through grid generation is to transform the problem into one of finding an intermediate mapping [12], which maps the original domain to a so-called computational domain, where it is simple to generate a uniform mesh. For this, we present two approaches: first, imposing minimum gradient energy mapping naturally leads to solving a system of Laplace-Beltrami partial differential equations [12], which offers robust efficiency in highly curved surfaces. Second, still within the mapping framework, optimal mass transportation has recently been proposed for grid generation under certain restrictions

Optics EXPRESS

[13,14]. Optimal mass transportation is a very active mathematical theory with significant optical applications [15].

Considering the diversity of problems exposed above, in this work, we propose and evaluate some surface discretization methods for optical aspheres. Our main motivation is to present a detailed analysis of several methods designed to optimize quality-based requirements based on uniformity, which fully addresses the influence of surface geometry.

This paper systematically studies three different strategies for surface discretization in optical aspheres. First, in section 2 we explain basic notions of surface discretization and quality measures. Second, in section 3 we present three optical archetypical aspheres used to evaluate the methods. In section 4, we present an algorithm that obtains the grid by constructing a circle involute embedded within the optical surface. Next, two methods based on finding an intermediate mapping are explained in section 5: one employing the Laplace-Beltrami operator (subsection 5.3) and the other the optimal mass transportation (subsection 5.4). For comparative purposes, we also implemented a trivial projection method (subsection 5.2). Section 6 presents a numerical comparative analysis of all the introduced surface discretization methods. Finally, in section 7 we discuss results and derive conclusions.

2. Surface discretization notions and quality metrics

The most general definition of surface discretization is an algorithm to specify points embedded over that surface, obeying some geometrical properties. The methods presented here generate a set of data points within the surface without a grid structure. However, to compute determined quality metrics, in a subsequent step, we created a grid from the point cloud. We employed an algorithm based on the classic surface reconstruction method called *crust* [16] available in [17], which produces a triangulated mesh surface from a point cloud.

Grid quality can be characterized considering certain features of the grid cells' boundaries, areas and/or elements of the surface metric tensor and their derivatives [12]. As an essential requirement, grid cells must not be folded or degenerate into lines or points. Also, cells should not differ too much from an equilateral curvilinear triangle. To quantify the difference compared to that reference equilateral triangle, we used the metric, taken from [18], given by the equation:

$$q = \frac{4\sqrt{3}A}{l_1^2 + l_2^2 + l_3^2}, \tag{1}$$

where l_i is the length of the i-th edge of the cell and A is the area of the triangle. We note that, in a flat geometry, q achieves its maximum value 1 only if the triangle is equilateral. Since we are dealing with curved triangles, we should compute l_i through geodesics, which would significantly increase computational cost. Instead, we approximated the curvilinear edges with straight lines, considering that the approximation is good enough when the grid cells are sufficiently small.

To evaluate the sampling uniformity, we divided the area of each triangle, A_i, by the mean triangle area, $\overline{A}$, over the whole grid: $A_i/\overline{A}$. We have also used these metrics to evaluate the sampling quality of data points generated through a curve embedded in the surface.

3. Asphere geometries

We tested our algorithms with three archetypical optical aspheres, which have been used for interlaboratory comparison with different metrological techniques [19]. The first asphere (from now on *weak asphere*) is taken from a Leica camera. The second surface is a *strong asphere* provided by Schneider GmbH & Co KG. Finally, the last example, produced by Thales Angenieux, is an extreme asphere containing a turning point connecting a convex part in the center and a concave annulus. Overall, the three aspheres represent a meaningful variety of possible designs that can be found in the market.

Optics EXPRESS

These surfaces are parameterized as $(x, y, Z(r))$, where $r = \sqrt{x^2 + y^2}$ and

$$Z(r) = \frac{r^2}{R\left(1 + \sqrt{1 - (1+\kappa)\frac{r^2}{R^2}}\right)} + c_4 r^4 + c_6 r^6 + c_8 r^8 + c_{10} r^{10} + c_{12} r^{12}, \tag{2}$$

being R the vertex radius of curvature, κ a conic constant and α_i coefficients describing the degree of asphericity. The parameters of each example are provided in Table 1 [19]. Plots of the three aspheres are shown in Fig. 1.

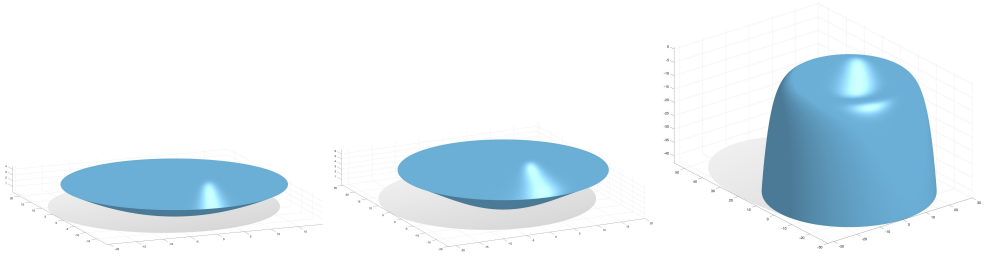

(a) (b) (c)

Fig. 1. The three aspheres used to test the surface discretization methods: (a) weak asphere; (b) strong asphere; and (c) turning point.

Table 1. Parameters of the three lens surfaces used in the numerics.

Parameter	Weak asphere	Strong asphere	Turning point
R (mm)	40.6193	20.097	94.6
κ	0	−1	−23.2046
α_4 (mm^{-3})	$-6.793\,75\times10^{-7}$	-2.0868×10^{-5}	$-6.864\,65\times10^{-6}$
α_6 (mm^{-5})	$-4.852\,03\times10^{-10}$	-3.9031×10^{-9}	$-1.218\,32\times10^{-8}$
α_8 (mm^{-7})	$-2.052\,23\times10^{-13}$	3.4102×10^{-11}	$2.224\,91\times10^{-11}$
α_{10} (mm^{-9})	-6.2324×10^{-17}	-3.2381×10^{-14}	$-8.060\,98\times10^{-14}$
α_{12} (mm^{-11})	-4.4857×10^{-20}	0	0
Diameter (mm)	39	40	60

4. Circle involute path scan embedded in an asphere

The method has already been explained elsewhere [20]. For completeness, we summarize it in the following. We start with a regular curve $\gamma : J \to \mathbb{R}^2$ defined on some interval $J \subset \mathbb{R}$. The coordinates in $\mathbb{R}^2$ are (x, z), and the curve can be written as $\gamma(s) = (\gamma_1(s), \gamma_2(s))$ for $s \in J$. Exclusively of this method, we consider the parameterization $\psi : J \times [0, 2\pi] \to \mathbb{R}^3$ of the asphere (given by Eq. (2)) obtained by rotating the curve γ around the z-axis:

$$\psi(s, \theta) = (\gamma_1(s)\cos\theta, \gamma_1(s)\sin\theta, \gamma_2(s)). \tag{3}$$

A geodesic, given by $\delta(t) := (s(t), \theta(t))$ parametrized with t, is uniquely determined by a set of second-order ordinary differential equations [21] and their initial values $\delta(0) = (s(0), \theta(0))$, $\delta'(0) = (s'(0), \theta'(0))$. After some computations [20], we obtained the equation of the involute

Optics EXPRESS

about the geodesic circle of radius s_0:

$$t \mapsto \delta_t(t) = \delta_0(t) + \left(0, tg(s_0)^{-1}\right) = \left(s(t), \theta(t) + tg(s_0)^{-1}\right),$$

where $g = \gamma_1^2$ The corresponding curve in the surface is given by:

$$t \longmapsto \psi\left(s(t), \theta(t) + tg(s_0)^{-1}\right).$$

Reducing the radius of the involute generating circle s_0 generates more sampling points. The surface associated with Eq. (2) is:

$$\gamma_1(s) = s,$$
$$\gamma_2(s) = s^2 R^{-1}\left(1 + \sqrt{1 - (1+\kappa)\frac{s^2}{R^2}}\right)^{-1} + c_2 s^2 + c_4 s^4 + c_8 s^8 + c_{10} s^{10} + c_{12} s^{12}.$$

Going back to the circle involute curve, the geodesic equations were solved numerically using a built-in MATLAB function: *ode45.m*, which generates a non-uniform distribution of points: (x_i, y_i, z_i), $i = 1, \ldots n$. Next, to obtain a uniform sampling along the geodesic, we interpolate those points imposing equal arc-length separation, with a step equal to $2\pi s_0$. The arc-length separation is approximately computed by $\delta_i \approx \sqrt{(x_{i+1} - x_i)^2 + (y_{i+1} - y_i)^2 + (z_{i+1} - z_i)^2}$.

The total length is $L = \sum_{i=1}^{n} \delta_i$, so a uniform arc-length step is given as $\delta_i = L/(n+1)$. We obtained the equal arc-length points on the curve (x_i, y_i, z_i), $i = 1, .., n$, by separately interpolating their s and θ parameters using spline interpolation. Specifically, we used the *interp1* MATLAB function with the *splines* option. Finally, the curve points were obtained by applying Eq. (3).

5. Grid generation based on intermediate mappings

Consider an optical surface Γ that is open, connected, and parameterized by $F : U \longrightarrow \Gamma$. Sometimes, grid generation algorithms are based on the computation of an intermediate mapping $T : Q \longrightarrow U$ satisfying certain geometrical properties [12]. Here, Q is a subset of the plane called *computational domain*. Usually, Q is chosen as the unit square, which provides a natural uniform Cartesian grid. However, we have chosen Q to be a circle due to the rotational symmetry of the optical aspheres. Then, this grid is mapped onto the surface Γ through T and F (Fig. 2).

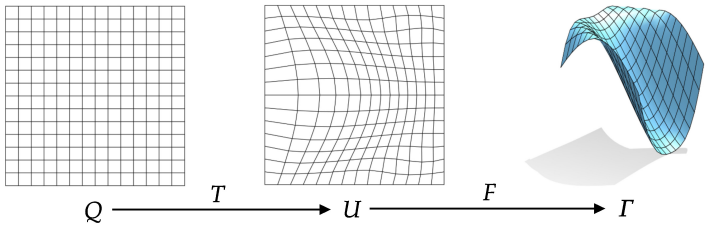

Fig. 2. Grid generation through an intermediate mapping.

Using this idea, we have implemented two grid generation methods: first, using the Laplace-Beltrami operator (section 5.3); and second, by optimal transport (section 5.4). We denote:

$$\begin{aligned} &F[x(\zeta)] : Q \subset \mathbb{R}^2 \to \Gamma \subset \mathbb{R}^3, \\ &T : Q \subset \mathbb{R}^2 \to U \subset \mathbb{R}^2, \quad \zeta = (\zeta_1, \zeta_2), \quad T(\zeta) = x(\zeta) = (x^1(\zeta_1, \zeta_2), x^2(\zeta_1, \zeta_2)), \end{aligned} \tag{4}$$

where F is the parameterization of the surface $F(x^1, x^2) = (x^1, x^2, Z(x^1, x^2))$, whose domain is another circle U. Then, the problem of finding the grid over the surface becomes searching for

Optics EXPRESS

a mapping T with certain properties. Note that $x(\zeta)$ must be one-to-one to avoid grid folding. Fortunately, as explained later, both the optimal transport method and the one based on the Laplace-Beltrami operator theoretically guarantee the generation of one-to-one mappings. The mapping must also obey that the boundary of Q maps onto that of U and subsequently of Γ.

5.1. Initial grid in the computational domain

The methods of intermediate mappings require an algorithm that efficiently generates uniform grids over the computational domain Q. This is trivial for Q being rectangular, but not for Q being a circle.

We propose a method that first generates a set of points through a circle involute curve [11] and then triangulates them. The arc-length parameterization of a circle with radius s_0 is $\alpha(t) = \left(s_0 \cos\left(\frac{t}{s_0}\right), s_0 \sin\left(\frac{t}{s_0}\right)\right)$. Then, the corresponding involute is given by

$$\beta(t) = \alpha(t) - t\alpha'(t) = \left(s_0 \cos\left(\frac{t}{s_0}\right) + t \sin\left(\frac{t}{s_0}\right), s_0 \sin\left(\frac{t}{s_0}\right) - t \cos\left(\frac{t}{s_0}\right)\right). \tag{5}$$

The arc-length reparameterization of the involute is $\tilde{\beta}(s) = \beta\left(\sqrt{2s_0 s}\right)$, which enables an equally spaced sampling $\tilde{\beta}(0)$, $\tilde{\beta}(2\pi s_0)$, $\tilde{\beta}(4\pi s_0)$, ... until the boundary of the circle is reached.

Subsequently, a mesh is generated from the points of the circle involute using a Delaunay triangulation, employing the function implemented in MATLAB `delaunay.m`. As shown in Fig. 3, this procedure generates a few triangles of low quality near the boundary. To avoid these boundary artifacts, we deleted triangles with a value q<0.75, where q is given in Eq. (1).

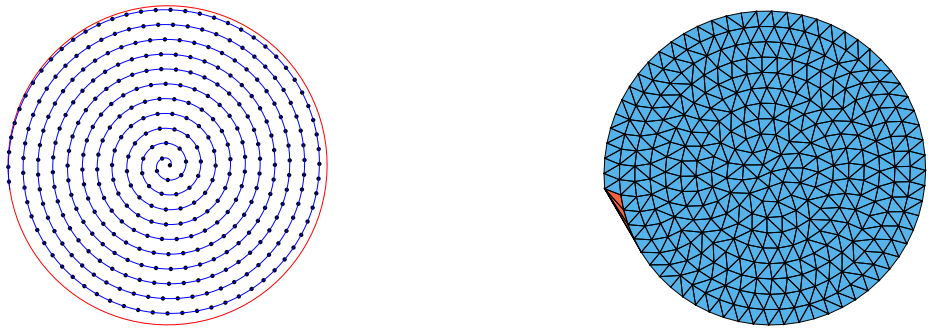

(a) (b)

Fig. 3. Grid generation example of the circular disk. (a) Points obtained from the circle involute parametrized by arclength. (b) Triangulation of previous points (using `delaunay.m`). Triangles with q<0.75 are colored red.

We have observed that this method generates meshes of comparable (or slightly better) quality than some other well-established grid generation methods, such as the so-called DistMesh method [22] or the grid generation algorithm implemented as part of MATLAB's PDE toolbox.

5.2. Grid generation with normal projection

The grid is generated by projecting the reference grid at the vertex plane onto the surface by projecting along the normal to that plane (z-axis). This is equivalent to using the identity as the intermediate mapping $x^1(\zeta_1, \zeta_2) = \zeta_1$, $x^2(\zeta_1, \zeta_2) = \zeta_2$.

5.3. Grid generation with Laplace-Beltrami operator

The crux of the Laplace-Beltrami method is not to obtain the mapping T directly [12], but its inverse $S = T^{-1} : U \longrightarrow Q$. This inverse mapping is obtained as a solution of the following

Optics EXPRESS

Laplace-Beltrami partial differential system [12]:

$$\begin{cases} \left(g^F\right)^{-\frac{1}{2}} \sum_{i,j} \partial_{x^j} \left(\sqrt{g^F} g_F^{ij} \partial_{x^i} S_k\right) = 0, & \text{in } U \\ S_k(x) = x^k, & \text{in } \partial U \end{cases} \tag{6}$$

where

$$g_{ij}^F(x) = \langle \partial_{x^i} F(x), \partial_{x^i} F(x) \rangle, \quad \left(g_F^{ij}(x)\right)_{ij} = \left(g_{ij}^F(x)\right)_{ij}^{-1}, \quad g^F = \det\left(g_{ij}^F(x)\right)_{ij}.$$

The Dirichlet boundary conditions are chosen so that the edges of the discs are fixed points of S and T. Equation (6) can be interpreted [12] as the minimization of:

$$\sum_k \int_\Gamma (\nabla S_k)^t G (\nabla S_k), \qquad G = \left(g_F^{ij}\right)_{ij}^{2\times 2},$$

which is a functional of smoothness, i.e., the integrated density and shape of the grid. The theory of harmonic maps [23] shows that $S : U \longrightarrow Q$ is one-to-one, ensuring that the grid does not fold. To numerically solve Eq. (6), each coordinate S_k was approximated with linear elements through the finite element algorithm implemented in MATLAB's PDE Toolbox [24]. Then S is linearly approximated when restricted to each finite element. This local linearization of each S_k allows for inverting the overall mapping $T = S^{-1}$ through straightforward linear algebra. Finally, the nodes of the surface grid in Γ are obtained employing the composition $F \circ T$. This may not be the most efficient way to generate a grid using Eqs. (6). However, this does not affect the analysis of Section 6.

5.4. Grid generation with optimal transport

To facilitate the analysis in this method, we have rescaled both Q and U to be the unit disc in $\mathbb{R}^2$. It has been previously shown [13] that optimal transport can be used to define grids that sample the plane with a prescribed density. In this method, given any curved region $R \subset \Gamma$, we have

$$C \cdot \text{Area}[(T \circ F)^{-1}(R)] = \text{Area}[R], \tag{7}$$

where $C>0$ is a proportionality constant, the left-hand side is the usual two-dimensional area in $Q \subset \mathbb{R}^2$ and

$$\text{Area}[R] = \int_{F^{-1}(R)} \sqrt{1 + Z'(r)}\, dx^1\, dx^2, \qquad r = \sqrt{(x^1)^2 + (x^2)^2}. \tag{8}$$

Note that the constant C is easily obtained as the area of the surface divided by the area of the computational domain (i.e., a disc). The mapping T is chosen so that it minimizes the functional

$$\int_Q |T(\zeta) - \zeta|^2 \, d\zeta.$$

subject to the constraint on Eq. (7). Intuitively, this selects an area-preserving mapping $Q \to \Gamma$ that minimizes the displacement $T(\zeta) - \zeta$. It can be proven that the optimal mapping is

$$T(\zeta_1, \zeta_2) = |\zeta|^{-1} \varphi(|\zeta|)\, (\zeta_1, \zeta_2), \quad \varphi : [0,1] \longrightarrow [0,1],$$

where the mapping φ solves a related optimal transport problem on the real line. That is, the optimal mapping only moves points in the radial direction. Moreover, the theory of optimal transport in one dimension [25] yields an explicit expression for φ.

$$\varphi(t) = \Phi^{-1}(t^2), \quad \Phi(t) = C_\Phi \int_0^t s\sqrt{1 + Z'(s)^2}\, ds, \quad C_\Phi = \left(\int_0^1 s\sqrt{1 + Z'(s)^2}\, ds\right)^{-1}. \tag{9}$$

The constant C_Φ is chosen so that Φ maps the interval $[0,1]$ to itself. Note that the previous formula for T shows that the mapping is one-to-one. Therefore, the resulting grid will not

Optics EXPRESS

self-intersect. In summary, to compute the mapping T, it is enough to compute the inverse of the primitive of a positive function. This has been achieved by approximating $s\sqrt{1+Z'(s)^2}$ with MATLAB's *spline.m* function, which enables the method to run in linear time.

6. Comparison between surface discretization methods

In this section, we provide qualitative and quantitative comparisons of the surface discretization methods described in sections 4 and 5 applied to the surface examples shown in section 3. From now on, we use the following acronyms: orthogonal projection (OP), Laplace-Beltrami (LB), optimal transport (OT), and circle involute (CI). Figures 4 and 5 respectively show the mesh surfaces generated by each method on the strong asphere and the asphere with a turning point. Additionally, Fig. 5 shows the data points before triangulation.

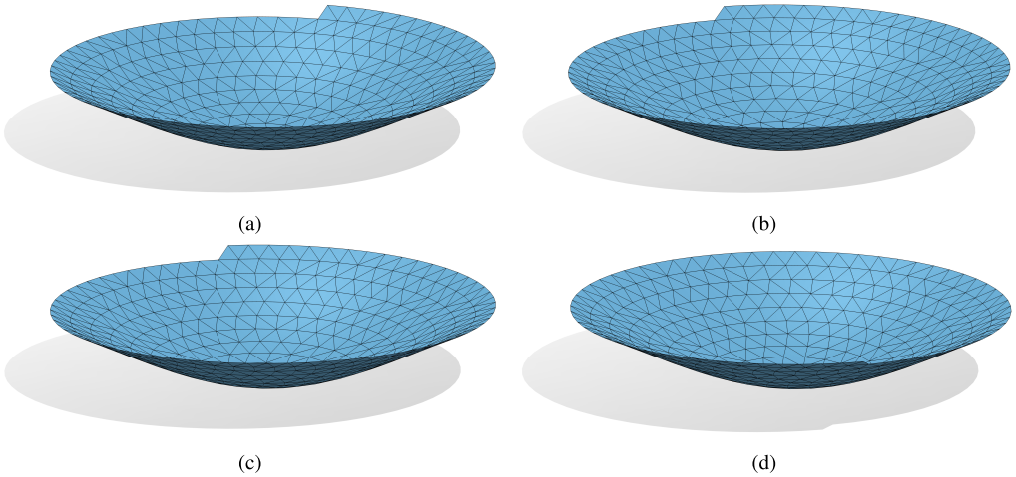

Fig. 4. Illustration of the grid generation methods on the strong asphere. (a) OP method; (b) LB method; (c) OT method, and (d) CI method.

By visual inspection, we observe that whereas the meshes generated by all methods do not differ significantly for the weak and strong aspheres, there are notable differences in the asphere with a turning point.

As expected, a simple visual inspection reveals that the OP method fails, compared with the rest of the methods, to generate a uniform discretization of the asphere with a turning point, especially in regions of rapid surface changes.

We evaluated the mesh uniformity and quality with the metrics described in section 2: $A_i/\overline{A}$ and q. We generated three grids with different numbers of data points. The number of points was indirectly determined by a parameter setting the mesh triangle edge length: h. Precisely, h is the edge's average length divided by the radius of the domain where the surface is defined. Particularly, we set $h = 0.05, 0.01, 0.005$. Both metrics depend on h. Figure 6 shows, through a boxplot, grid cell analysis (a graphical representation of statistical data) the dependence of $A_i/\overline{A}$, and Fig. 7 shows the dependence of q.

Figures 6(a) and 6(b) show that all methods produce reasonably uniform grids for the weak and strong aspheres. About 50% of all triangles have an area between $0.95\overline{A}$ (mean area of a triangle) and $1.05\overline{A}$. Still, the CI and OT methods produce significantly more uniform grids.

The differences between methods are sharper when observing the asphere with a turning point, as shown in Fig. 6(c). Whereas, when using the CI and OT methods, the triangle's areas are closely concentrated around the mean, in the LB and OP methods, there is a much higher dispersion, with about 50% of the triangles having areas under $0.6\overline{A}$.

Optics EXPRESS

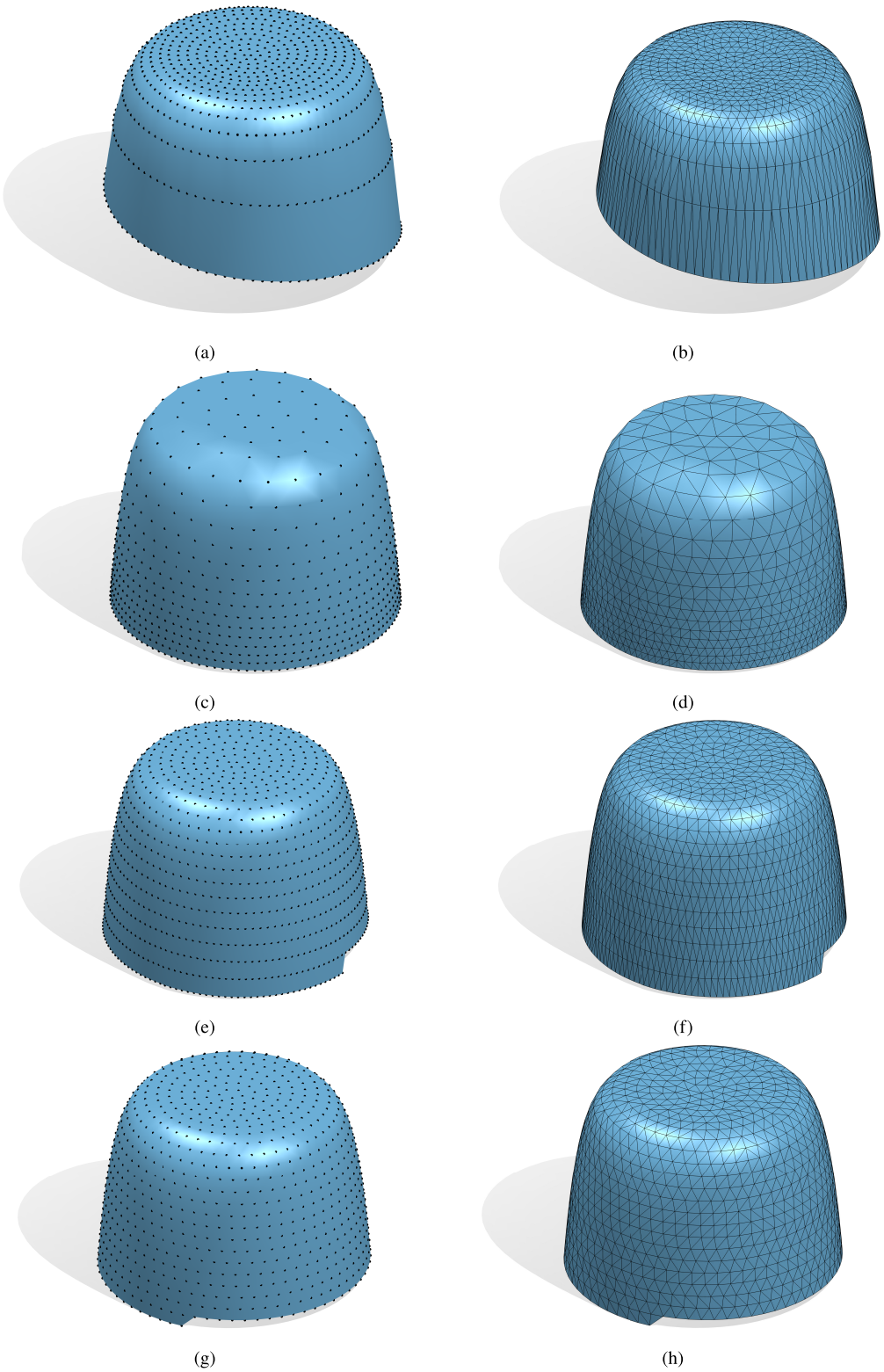

Fig. 5. Illustration of the grid generation methods on the asphere with a turning point. The left column represents data points, whereas the right one shows the triangulation meshes. (a-b) OP method; (c-d) LB method; (e-f) OT method, and (g-h) CI method.

Optics EXPRESS

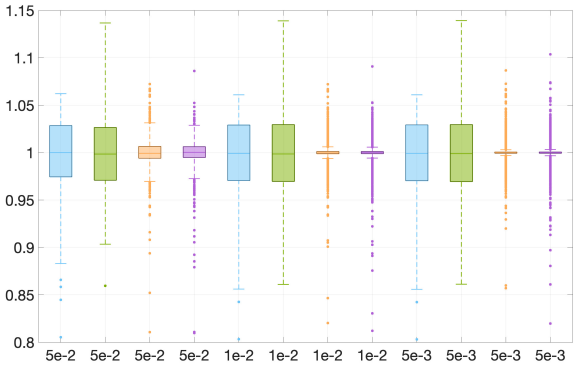

(a)

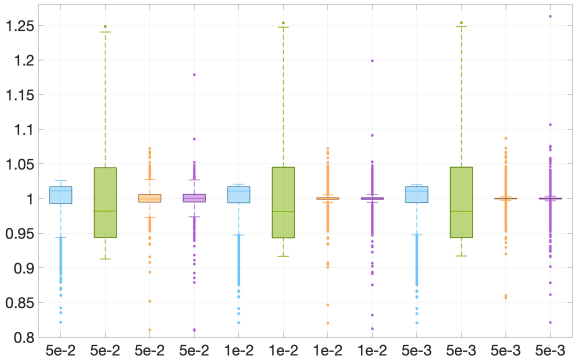

(b)

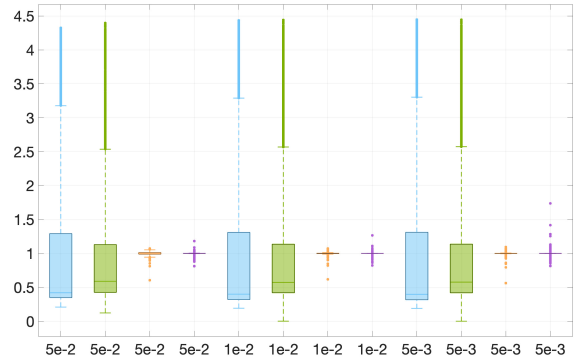

(c)

Fig. 6. Boxplots of the area of each triangle divided by the mean area for the involute method (blue), the Laplace-Beltrami method (green), the projection method (purple), and the optimal transport method (orange) for different relative lengths (h). Analysis of: (a) weak asphere, (b) strong asphere, and (c) turning point asphere.

Optics EXPRESS

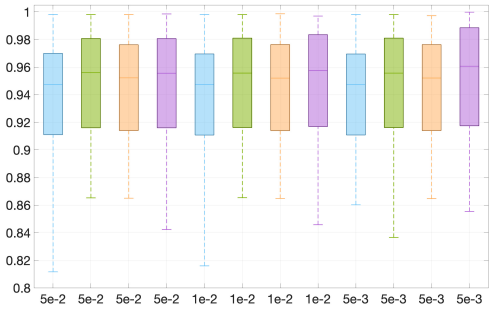

(a)

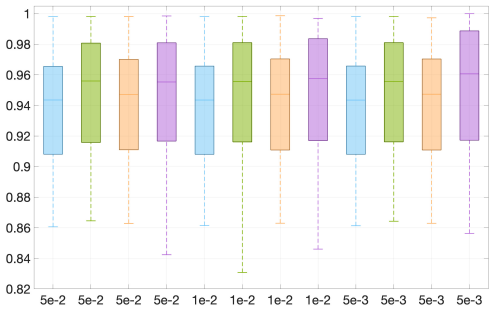

(b)

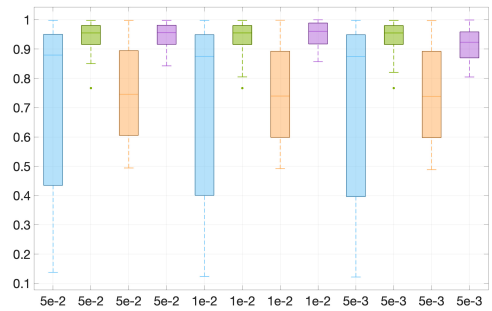

(c)

Fig. 7. Boxplots of the quality metric q for the involute method (blue), the Laplace-Beltrami method (green), the projection method (purple), and the optimal transport method (orange) for different relative grid cell lengths (h). Plots for: (a) weak asphere, (b) strong asphere, and (c) turning point asphere.

We also observe a strong presence of outliers in every plot of Fig. 6, corresponding to a set of triangles with an abnormally large or minor area. Figures 8(c) and 8(d) show that, for the CI and OT methods, these triangles are concentrated in spirals near the center of the surface. On the other hand, Figs. 8(a) and 8(b) show that OP generates abnormally large triangles near the surface's boundary, whereas the LB method generates them close to the center.

The mesh quality, through metric q, is analyzed in Fig. 7. Figures 7(a) and 7(b) show that all the methods produce similar values of q for the weak and strong aspheres, with a percentage of

Optics EXPRESS

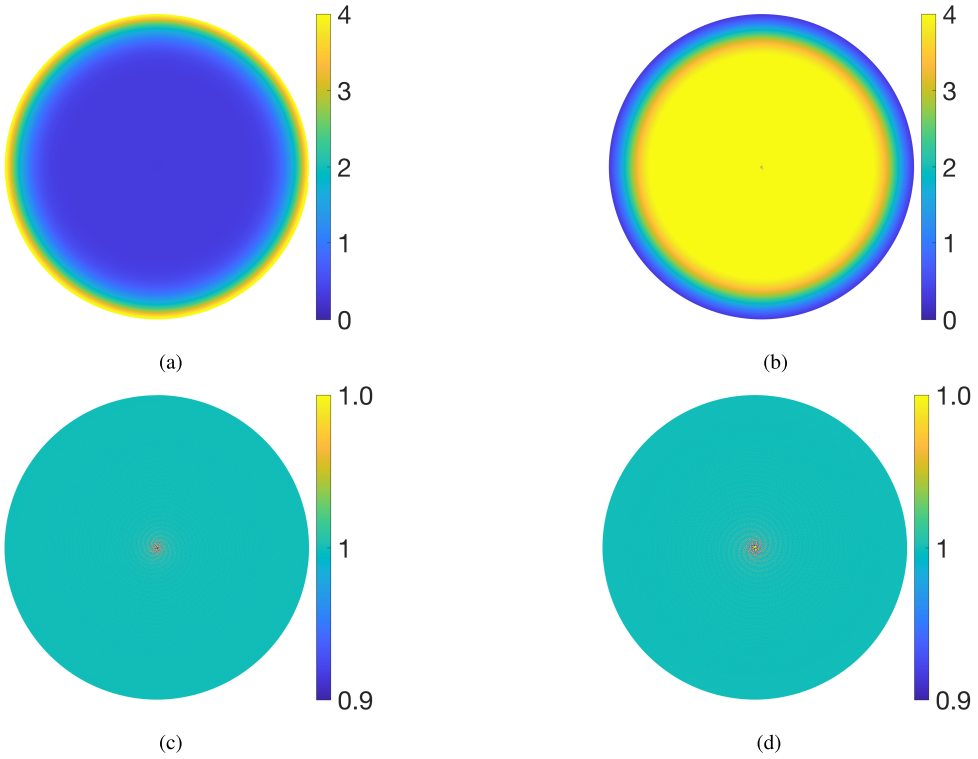

Fig. 8. Heatmap of triangle area divided by mean area across the turning point asphere: (a) OP, (b) LB, (c) OT, and (d) CI methods

triangles having q>0.9 greater than 75%. In any case, CI and LB produce slightly better-quality triangles than OP and OT methods.

However, in Fig. 7(c), we can see great differences between the methods for the asphere with a turning point. The CI and LB methods still retain a percentage of triangles with q>0.9 greater than 75%. On the other hand, in the OT method, we observe that more than 50% of the triangles have q<0.8. In addition, OP has a highly asymmetric distribution of values of q.

We have also evaluated the distribution of the quality metrics across the entire surface for the turning point example. Figure 8 shows the distribution of $A_i/\bar{A}$, while Fig. 9 shows the distribution of q. While the values of $A_i/\bar{A}$ are uniform across the surface for the OT and CI methods, Figs. 8(a) and 8(b) show a high variation for the OP and LB methods. Indeed, for a better visualization, we had to clip the interval colormap range to $[0, 4]$. In the OP method, we observe the presence of triangles with abnormally large areas near the boundary and, contrary to the LB method, small triangles at the center of the surface.

Both the OT and OP exhibit triangles of significantly lower quality near the boundary. Conversely, the CI and OT grids are highly uniform except for a few triangles following a spiral pattern near the center, corresponding to the outliers from Fig. 6. The presence of these artifacts is clearer in the spatial distribution of q, as shown in Fig. 9. The value of q is quite stable across the whole surface, although some spiral patterns of differing quality values appear in all methods. These are probably due to the triangulation procedure.

Optics EXPRESS

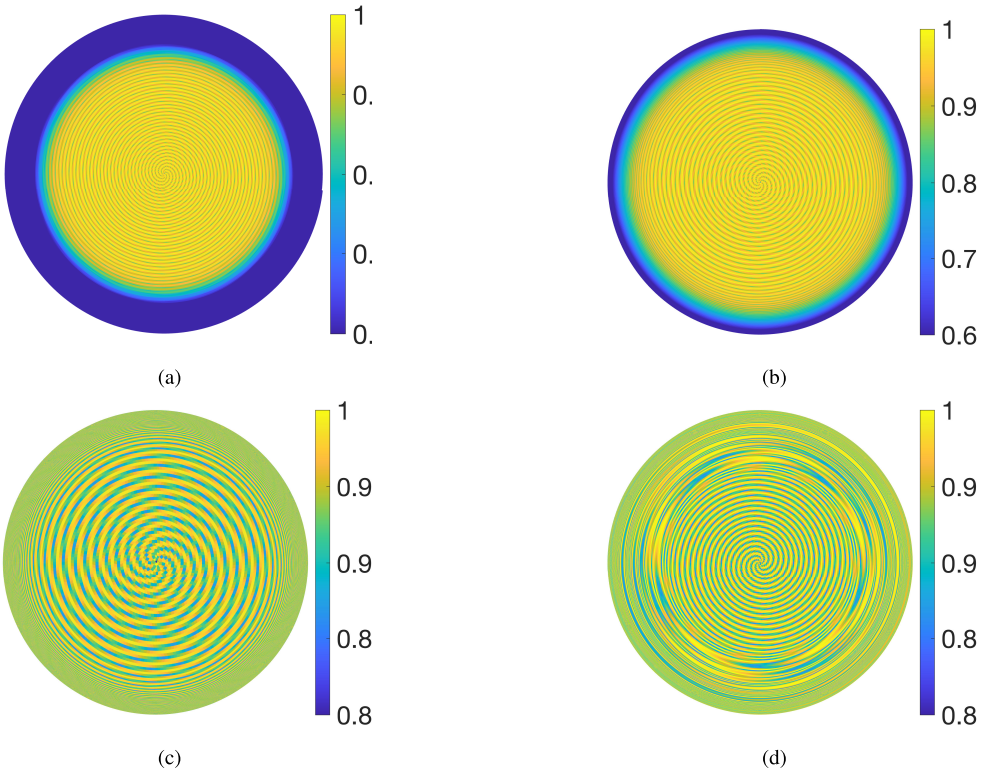

Fig. 9. Heatmap of the quality measure q across the turning point asphere: (a) OP, (b) LB, (c) OT and (d) CI methods

6.1. *Dependence of surface discretization on surface geometry*

As mentioned before, the performance of the surface discretization may be affected by surface geometry, and this dependence is higher in the projection method than in the others. Also, when the surface geometry tends to be planar, all the methods should converge to the same result. To further analyze the influence of surface geometry, we evaluated the quality metrics when using a sphere of varying radius of curvature as a test. We particularly considered spherical surface portions –defined in a circular domain of radius one– with increasing radius of curvature.

Figure 10 provides the standard deviation of $A_i/\overline{A}$ and the mean value of q as a function of the radius of curvature of the sphere. The q quality metric is quite stable against variations in the radius of curvature for the CI and LB methods, but that is not the case for OP and OT. Conversely, when analyzing $A_i/\overline{A}$, the only stable methods against variation in the radius of curvature are CI and OT.

6.2. *Theoretical comparison between the CI and OT methods*

We also explored the theoretical connection between the CI and OT methods. For this purpose, we analytically compared the location of a point close to the edge obtained with both methods (these have almost explicit formulas). Specifically, we analyzed the limit behavior of the ratio of point locations with increasing grid density.

For simplicity, set $s_1 = 2s_0$, the diameter of the moving circle in the CI method. In the OT approach, fix a point in the computational domain (unit disk), say ζ_*, that lies a distance s_1 from the boundary. That is, $|\zeta_*| = 1 - s_1 =: t_1$. The OT maps this point onto a point

Optics EXPRESS

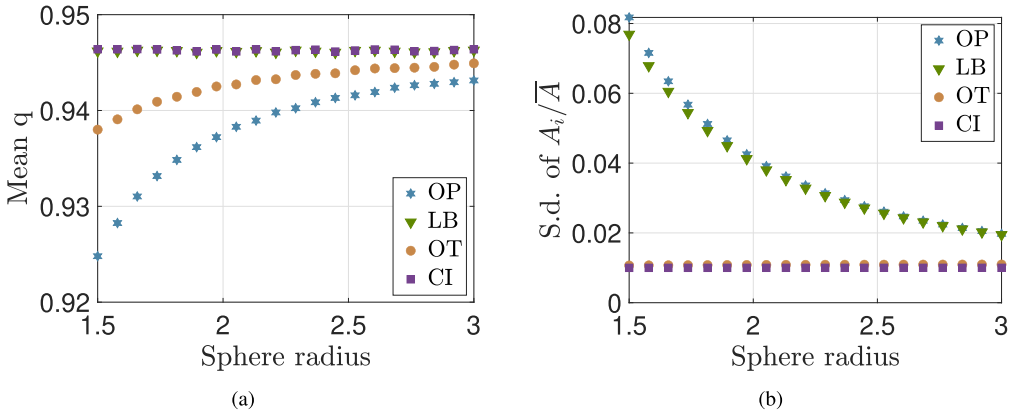

Fig. 10. Behavior of the surface discretization methods on spheres of increasing radius. (a) Mean value of q; (b) Standard deviation of $A_i/\overline{A}$.

$T(\zeta_*) = |\zeta_*|^{-1}\varphi(t_1)\zeta_*$ in $\mathbb{R}^2$, which has norm

$$|T(\zeta_*)| = \varphi(t_1) = \varphi(1 - s_1).$$

Then, the point with x-y coordinates $T(\zeta_*)$ and vertical height $Z(|T(\zeta_*)|)$, denoted by P_*, belongs to the grid on the surface.

We compare the location of this point P_* with a corresponding point in the grid obtained by the CI. For this purpose, we calculate the distance in $\mathbb{R}^3$ from P_* to the boundary of the surface, which is given by

$$d_* = \sqrt{(1 - |T(\zeta_*)|)^2 + Z(|T(\zeta_*)|) - Z(1)^2}.$$

In the CI method, this distance would be approximately s_1, that is, the Euclidean distance in the tangent plane at each point of the surface.

To compare both, calculate:

$$\begin{aligned}\gamma := \lim_{s_1\to 0}\frac{d_*}{s_1} &= \lim_{s_1\to 0}\frac{\sqrt{(1-\varphi(1-s_1)^2 + (Z(\varphi(1-s_1)) - Z(1))^2}}{s_1}\\ &= \lim_{s_1\to 0}\sqrt{\left(\frac{1-\varphi(1-s_1)}{s_1}\right)^2 + \left(\frac{Z(\varphi(1-s_1)) - Z(1)}{s_1}\right)^2}\\ &= \sqrt{\varphi'(1)^2 + Z'(\varphi(1))^2\varphi'(1)^2}.\end{aligned}$$

On the other hand,

$$\varphi'(t) = 2t(\Phi^{-1})'(t^2) = 2t[\Phi'(\Phi^{-1}(t^2))]^{-1} = \frac{2t}{C_\Phi}\left(\Phi^{-1}(t^2)\sqrt{1 + Z'(\Phi^{-1}(t^2))^2}\right)^{-1},$$

so that $\varphi'(1) = \frac{2}{C_\Phi}\frac{1}{\sqrt{Z'(1)^2+1}}$, and we can conclude:

$$\gamma = 2/C_\Phi. \tag{10}$$

Equation (10) establishes that the geometry of the surface globally determines the relationship between the CI and the OT methods. A simple computation shows that γ is equal to the total area of the surface divided by π, which is also the proportionality constant found in Eq. (8).

Optics EXPRESS

Consequently, higher surface area causes a bigger discrepancy between the methods. Note also that γ can be thought of as a measure of how the OT method stretches the radial location of points near the edge of the surface compared to the CI method. This affects the shape of the triangles, and consequently their q values, but not its uniformity measure as shown in Fig. 10.

In the case of planar geometry ($Z \equiv 0$, which yields $\gamma = 1$) both methods provide the same point. For the three examples used, we computed the following values of γ that exemplify this interpretation: weak asphere ($\gamma = 1.06$), strong asphere ($\gamma = 1.09$), and turning point ($\gamma = 3.22$).

7. Discussion

When surface discretization is performed in aspheres containing significant curvatures and/or curvature variations, such as optical aspheres with turning points, the conventional projection method fails at providing a uniform point distribution. We have presented three alternative methods that are more convenient in these cases. First, one based on computing circle involutes embedded within the surface (CI); second, a method that solves a Laplace-Beltrami system of equations (LB); and third, one that uses optimal transport of a uniform mesh generated in the vertex plane with a circle involute (OT).

We have proved that the CI and OT methods provide the best outcomes if uniformity is targeted. Moreover, our discussion above indicates that, theoretically, both methods converge when the surface flattens. However, if the criterion is to have grid cells close to equilateral, then LB and CI would be the best methods. A disadvantage of the LB method is its computational cost. One is forced either to generate a planar grid to solve the system directly or to use an iterative algorithm to solve the nonlinear inverted PDE system [12]. Two aspects make the OT method appealing for some applications. Firstly, it is as fast as the projection method. Second, it can be adapted to surface metrics with non-uniform area one. For instance, in some optical applications, the goal is not to sample uniformly on the surface area but rather in the curvature distribution or its variation.

Although in this paper we characterize uniformity through a post-triangulation procedure, the main objective of the proposed methods is to generate a set of data points, not necessarily associated with any particular triangulation, discretizing the surface. In contrast, successful mesh generation algorithms such as the two-dimensional DistMesh [22] algorithm determine the location of data points intrinsically considering the grid cell construction. Therefore, we attribute the mesh artifacts described in section 6 to the sequential application of the triangulation using the Crust algorithm [17] to the non-grid dependent methods of surface discretization.

In future work, we plan to generalize and adapt the methods shown in this paper to nonaxially symmetric optical surfaces, such as free-form surfaces, which are undergoing a boom in optics [26]. In the case of the involute method, this requires some extra computational effort because computing geodesics in non-rotationally symmetric surfaces is not as straightforward as in rotationally symmetric ones. Although there are different algorithms for this scenario (see, e.g. [27] and references there), all of them imply higher computational cost and lower accuracy, as compared with the rotationally symmetric case. Even greater difficulties would be encountered when generalizing the OT method to non-axially symmetric surfaces because, in that case, the mass transportation problem cannot be reduced to a one-dimensional problem. Then, the most direct way to tackle the problem is to look for solutions to the two-dimensional Monge-Ampere equation. However, this is a fully nonlinear partial differential equation, which cannot be solved efficiently with the usual finite element methods. We also plan to develop grid generation methods that consider geometrical features, for instance, a third-order smoothness metric [28].

Funding. Ministerio de Ciencia, Innovación y Universidades (s PID2020-113596GB-I0, PID2023-150166NB-I00, RED2022-134784-T).

Acknowledgments. This work was supported by grants PID2020-113596GB-I00, PID2023-150166NB-I00, RED2022-134784-T, all funded by MCIN/AEI/10.13039/501100011033. We thank Manuel Ritore for his ideas related to the circle involute method.

Optics EXPRESS

Disclosures. The authors declare no conflict of interest.

Data availability. No data were generated or analyzed in the presented research.

References

1. A. Beutler, "Metrology for the production process of aspheric lenses," Adv. Opt. Technol. **5**(3), 211–228 (2016).
2. A. Müller, C. Falldorf, and R. Bergmann, "Approaching optical metrology with multiple light sources and compressive sensing," in *Optics and photonics for advanced dimensional metrology II*, vol. 12137 (SPIE, 2022), pp. 121370L1–8.
3. R. Tutsch and H. Dierke, "Evaluation of different sampling strategies for pointwise measurement of aspheric surfaces," in *SPIE Conference Series*, vol. 12607 (2023), pp. 126070H 1–8.
4. G. Lee, J. Mou, and Y. Shen, "Sampling strategy design for dimensional measurement of geometric features using coordinate measuring machine," Int. J. Mach. Tools Manuf. **37**(7), 917–934 (1997).
5. C. E. Collins, E. B. Fay, J. A. Aguirre-Cruz, *et al.*, "Alternate methods for sampling in coordinate metrology," Proc. Inst. Mech. Eng., Part B **221**(6), 1041–1052 (2007).
6. M. Wieczorowski, "Spiral sampling as a fast way of data acquisition in surface topography," Int. J. Mach. Tools Manuf. **41**(13-14), 2017–2022 (2001).
7. J. Wagner, D. Goldblum, and P. C. Cattin, "Golden angle based scanning for robust corneal topography with oct," Biomed. Opt. Express **8**(2), 475–483 (2017).
8. R. Balasubramaniam, R. V. Sarepaka, and S. Subbiah, *Diamond turn machining: theory and practice* (CRC Press, 2018).
9. R. Edgeworth and R. G. Wilhelm, "Adaptive sampling for coordinate metrology," Precis. Eng. **23**(3), 144–154 (1999).
10. H. Gong, Y. Wang, L. Song, *et al.*, "Spiral tool path generation for diamond turning optical freeform surfaces of quasi-revolution," Comput. Aided Des. **59**, 15–22 (2015).
11. S. Barbero and M. Ritoré, "Circle involute as an optimal scan path, minimizing acquisition time, in surface topography," Surf. Topogr.: Metrol. Prop. **7**, 1933–1939 (2019).
12. V. D. Liseikin, *Grid generation methods. III edition*. (Springer, 2017).
13. J. M. Finn, G. L. Delzanno, and L. Chacón, "Grid generation and adaptation by monge-kantorovich optimization in two and three dimensions," in *Proceedings of the 17th International Meshing Roundtable*, R. V. Garimella, ed. (Springer, 2008), pp. 551–568.
14. G. Delzanno, L. Chacón, J. Finn, *et al.*, "An optimal robust equidistribution method for two-dimensional grid adaptation based on Monge–Kantorovich optimization," J. Comput. Phys. **227**(23), 9841–9864 (2008).
15. C. E. Gutiérrez, *Optimal transport and applications to geometric optics* (Springer, 2023).
16. N. Amenta, M. Bern, and M. Kamvysselis, "A new voronoi-based surface reconstruction algorithm," in *Proceedings of the 25th annual conference on Computer graphics and interactive techniques*, (1998), pp. 415–421.
17. L. Giaccari, "Surface reconstruction from scattered points cloud," MATLAB Central File Exchange (https://www.mathworks.com/matlabcentral/fileexchange/63730-surface-reconstruction-from-scattered-points-cloud) (2024).
18. D. Field, "Qualitative measures for initial meshes," Int. J. Numer. Meth. Engng. **47**(4), 887–906 (2000).
19. R. Schachtschneider, I. Fortmeier, M. Stavridis, *et al.*, "Interlaboratory comparison measurements of aspheres," Meas. Sci. Technol. **29**(5), 055010 (2018).
20. S. Barbero and M. Ritoré, "Extended-depth-of-focus wavefront design from pseudo-umbilical space curves," J. Opt. Soc. Am. A **40**(10), 1933–1939 (2023).
21. D. J. Struik, *Lectures on classical differential geometry* (Dover, 2003).
22. P. O. Persson and G. Strang, "A simple mesh generator in matlab," SIAM Rev. **46**(2), 329–345 (2004).
23. J. Jost, "Univalency of harmonic mappings between surfaces," Journal fur reine Angew. Math. pp. 141–153 (1981).
24. MATLAB Toolbox "Partial differential equation toolbox," MATLAB Help Center (2025), https://es.mathworks.com/help/pde/
25. F. Santambrogio, *Optimal transport for applied mathematicians. Calculus of variations, PDEs, and modeling* (Springer, 2015).
26. J. P. Rolland, M. A. Davies, T. J. Suleski, *et al.*, "Freeform optics for imaging," Optica **8**(2), 161–176 (2021).
27. K. Crane, M. Livesu, E. Puppo, *et al.*, "A survey of algorithms for geodesic paths and distances," arXiv (2007).
28. S. Barbero, "Third-order smoothness metric to characterize progressive addition lenses," J. Opt. Soc. Am. A **41**(8), 1554–1562 (2024).